Elaborating the Crystal Structures of MgAgSb Thermoelectric Compound: Polymorphs and Atomic Disorders

Jian-Li Mi,*,[†] Ping-Jun Ying,[‡] Mattia Sist,[§] Hazel Reardon,[§] Peng Zhang,[†] Tie-Jun Zhu,*,[‡] Xin-Bing Zhao,[‡] and Bo Brummerstedt Iversen*,[§]

[†]Institute for Advanced Materials, School of Materials Science and Engineering, Jiangsu University, Zhenjiang 212013, China

[‡]State Key Laboratory of Silicon Materials and School of Materials Science and Engineering, Zhejiang University, Hangzhou 310027, China

[§]Center for Materials Crystallography, Department of Chemistry and iNANO, Aarhus University, DK-8000, Aarhus C., Denmark

Ⓢ *Supporting Information*

ABSTRACT: Gaining insight into crystal structure is essential for understanding thermoelectric transport mechanisms and predicting thermoelectric properties. The main challenge in studying thermoelectric mechanisms is often imprecise or wrong models of the crystal structure. This work examines the structure modifications observed in MgAgSb thermoelectric materials by multitemperature high-resolution synchrotron radiation powder X-ray diffraction (SR-PXRD). Rietveld refinement reveals large atomic displacement parameters (ADPs) of the Ag1 atoms at the $4a$ position indicating possible atomic disorder, which may contribute to the low thermal conductivity observed in α-MgAgSb. The temperature dependence
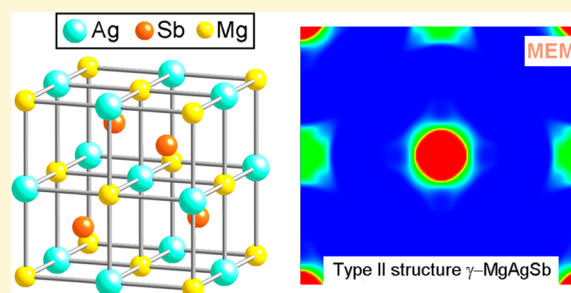
of anisotropic structural parameters indicates a tendency of increasing structural symmetry in α-MgAgSb with increasing temperature, largely contributing to the temperature evolution of the thermoelectric properties. Two MgAgSb polymorphs (β-MgAgSb and γ-MgAgSb) coexist at 700 K, and only the γ-MgAgSb crystalline phase is found at high temperatures (800−1000 K). The content of γ-MgAgSb phase decreases with temperature due to the increase of liquid impurities, and the sample is only 43.8% crystalline at 1000 K. At 800 K, the high resolution powder data are fitted equally well using type I (with Mg, Ag, and Sb on the $4b$, $4c$, and $4a$ sites, respectively) and type II (with Mg, Ag, and Sb on the $4a$, $4b$, and $4c$ sites, respectively) half-Heusler crystal structure models. Nonetheless, maximum entropy method (MEM) analysis carried out on the extracted factors shows that the type II structure gives a more physically sound MEM electron density. The disorder in γ-MgAgSb consists of mixed sites of Mg and Ag as well as vacancies, and the strong disorder of the cation sublattice contributes to the low thermal conductivity.

1. INTRODUCTION

Thermoelectric materials have attracted considerable attention as one of the potential candidates for alternative energy sources based on their ability to convert heat to electricity or vice versa.[1,2] The conversion efficiency of thermoelectric materials is represented by the dimensionless figure of merit $zT = (\alpha^2\sigma/\kappa)T$, where α, σ, κ, and T are the Seebeck coefficient, the electrical conductivity, the thermal conductivity, and the absolute temperature, respectively. Continuous efforts have been devoted to developing new materials and improving thermoelectric performance.[3−6] MgAgSb-based materials have been reported with a figure of merit larger than unity near room-temperature.[7−9] The intrinsically weak electron−phonon coupling contributes to the high power factor of MgAgSb.[10] In our previous study, we have shown a high zT of ~1.1 at 525 K in In-doped MgAgSb.[11] The hierarchical weak chemical bonds were suggested to be responsible for the intrinsically low thermal conductivity in MgAgSb.[12]

Detailed knowledge of the crystal structure is required to understand the thermoelectric properties. MgAgSb is known to

exist in three different polymorphs: a tetragonal α phase (space group $I\text{-}4c2$) at low temperatures, a Cu_2Sb-related β phase (space group $P4/nmm$) at intermediate temperatures, and a half-Heusler γ phase (cubic, space group $F\text{-}43m$) at high temperatures.[13] The structure−property relationships of MgAgSb are still poorly understood, and previous studies do not provide consistent thermoelectric property information for MgAgSb, where the deviation between theoretical and experimental studies is evident.[13−15] On one hand, phase pure MgAgSb is typically difficult to achieve, and therefore, the thermoelectric properties may be considerably influenced by residual impurities, for example, α-MgAgSb with impurities produces a maximum $zT \approx 0.5$.[13] Zhao et al. found that phase pure α-MgAgSb has a much improved zT of >1.[14] The thermoelectric properties can be further improved by doping, and a peak $zT \approx 1.4$ was achieved by doping with low

concentrations of Ni, highlighting α-MgAgSb based material as a very promising candidate for thermoelectric applications.[14] On the other hand, the imprecise understanding of the crystal structure may be the origin of the discrepancy between the calculated and measured thermoelectric properties. Miao et al. predicted the Seebeck coefficients of MgAgSb, and it was found that the evolution of the calculated Seebeck coefficients with temperature cannot fully explain the experimentally observed values, especially for the high temperature γ phase.[15] Theoretical calculations show that γ-MgAgSb has a metallic character, while experimental studies suggest that it behaves as a semiconductor. Generally, the thermoelectric properties are strongly sensitive to the crystal structure; thus, the structure evolution with temperature is important for predicting the temperature dependence of the properties. The macroscopic quantities such as Seebeck coefficient and electronic conductivity are directly related to the electronic states, which are defined by the crystal structure of a material. Clearly gaining accurate information on the crystal structure is of great importance for understanding the thermoelectric mechanisms and predicting the thermoelectric properties reliably.[16] Therefore, in the present case, there is significant motivation for us to further investigate the phase purities, crystal structures, and possible structural disorder in the different MgAgSb polymorphs at different temperatures.

High-resolution synchrotron radiation powder X-ray diffraction (SR-PXRD) is a convenient and powerful method to investigate detailed crystal structures. The atomic displacement parameters (ADPs) represent the atomic thermal vibration, but in addition they may contain contributions from static and dynamic disorders. Therefore, SR-PXRD can also be used to analyze structural disorder, and SR-PXRD methods have been used to interpret disorder in clathrates,[17] skutterudites,[18] PbTe,[19] Zn_4Sb_3,[20] and ZrNiSn based alloys.[21] Nevertheless, in most cases, the interpretation of subtle atomic disorder remains challenging, and usually requires more advanced analysis methods than Rietveld refinement. The maximum entropy method (MEM) has been used to obtain elaborate charge density visualization of SR-PXRD data, revealing anharmonicity and large cation disorder in PbTe and PbS.[19] In all cases, the information about atomic disorder is specifically contained in the high-order data region, and therefore, high energy synchrotron radiation is required to obtain data of sufficient quality for accurate results.

In this work, high purity MgAgSb samples were carefully prepared, and the detailed structures of MgAgSb polymorphs were studied by multitemperature SR-PXRD. The analysis shows that the presence of weak chemical bonds and large atomic disorder contributes significantly to the intrinsically low thermal conductivity of α-MgAgSb. A tendency of increased structural symmetry is observed for α-MgAgSb with increasing temperature. The structure and structural disorder of γ-MgAgSb are comprehensively discussed in light of different possible structural models. Moreover, MEM analysis was carried out to further scrutinize the different structural models. Finally, the thermoelectric properties of different MgAgSb polymorphs were thoroughly presented.

2. EXPERIMENTAL METHODS

Mg (99.9%, powder, Alfa Aesar), Ag (99.9%, powder, Alfa Aesar), and Sb (99.999%, powder, Alfa Aesar) were weighted according to the nominal composition MgAgSb and then loaded into a stainless steel jar with balls in the argon-filled glovebox. The materials were ball-milled

for 90 min and then sintered with a spark plasma sintering system (SPS-1050, Sumitomo Coal Mining Co.) under an axial compressive stress of 60 MPa in vacuum at 700 K for 6 min, which resulted in a disk-shaped sample of ϕ12.6 mm $\times$ 2 mm. The obtained sample was sealed inside an evacuated quartz tube and annealed at 553 K for 2 weeks to form pure α-MgAgSb phase. More synthesis details can be found elsewhere.[11]

To ensure a homogeneous particle size of the sample for the SR-PXRD measurement, the finely ground powder was floated in ethanol three times. The floated powders were then transferred to 0.2 mm quartz capillaries to obtain a dense packing of the powder. The SR-PXRD data were collected at temperatures from 300 to 1000 K in steps of 100 K, at beamline BL44B2 at SPring-8, Japan.[22] The wavelength (λ = 0.500249 Å) was determined from data measured on a CeO_2 standard (a = 5.411102 Å). Rietveld refinements at all temperatures were carried out using the FULLPROF[23] and Jana2006[24] programs using a pseudo-Voigt peak shape. The background was modeled using linear interpolation between a set of background points with refinable heights in refinements carried out with FULLPROF, while manually selected background points interpolated by fifth order Chebyshev Polynomials were used in Jana2006.

Structure factors on absolute scale extracted according to the Rietveld refinement model were used to compute maximum entropy method (MEM)[25] electron densities. The Sakata-Sato formalism[25] with a flat uniform prior density as implemented in the BayMEM software[26] was used, and the unit cell was divided into 128 $\times$ 128 $\times$ 128 pixels. The aim χ^2 was set to 1, and the calculations were stopped after 100 000 cycles if χ^2 = 1 could not be reached.

Differential scanning calorimetry (DSC) measurements were done with a SDT Q600 V20.9 Build 20 thermoanalyzer in helium atmosphere with a heating rate of 10 K/min. The thermal conductivity was calculated from $\kappa = D\rho C_p$, where the density (ρ) was estimated by an Archimedes method, the thermal diffusivity coefficient (D) was measured using the laser flash method in a Netzsch LFA457 instrument, and the specific heat capacity (C_p) was derived using a Pyroceram standard (Pyroceram 9606) in the range of 300−700 K. The electrical conductivity and the Seebeck coefficient in the temperature range between 300 and 700 K were measured in a vacuum using a DC four-probe method and differential voltage/temperature technique with the sample dimensions of 12 mm $\times$ 3 mm $\times$ 2 mm.[27]

Density functional theory calculations (DFT) were performed with Quantum Espresso (QE)[28] at various unit cell volumes. The projector augmented wave (PAW) method[29] was used to describe the potential due to the core electrons and nucleus combined, the kinetic energy cutoff for the wave function and for the charge density were set to 32 and 165 Ry, respectively. For the exchange-correlation functional, the generalized gradient approximation (GGA) of Perdew−Burke−Ernzerhof (PBE)[30] was used. The 8 $\times$ 8 $\times$ 8 K points for Brillouin zone sampling were used. Phonon calculations were performed using the ph.x code of QE using the linear response method,[31] where 8 $\times$ 8 $\times$ 8 K points for Brillouin zone sampling and a grid of 4 $\times$ 4 $\times$ 4 q-points in reciprocal space were used. Band structure calculations were performed with QE at the optimized geometries using the band.x code, and 16 $\times$ 16 $\times$ 16 K points for Brillouin zone sampling were used. The phonon dispersion and band structure were computed along a specific symmetry path in K-space of the unit cell according to Setyawan and Curtarolo.[32]

3. RESULTS AND DISCUSSION

3.1. Structural Refinement. Similar to the report by Kirkham,[13] three different crystal structures are found during the heating of the MgAgSb sample. The multitemperature SR-PXRD data show that the low temperature phase (α-MgAgSb) is stable up to 600 K, the intermediate phase (β-MgAgSb) and high temperature phase (γ-MgAgSb) coexist at 700 K, and only γ-MgAgSb phase is found $\geq$800 K. In all three phases, the Mg and Sb atoms form either distorted or undistorted Mg−Sb

rocksalt-type sublattices. Figure 1 shows the three different structures with Ag atoms located on half of the Mg−Sb polyhedron sites.
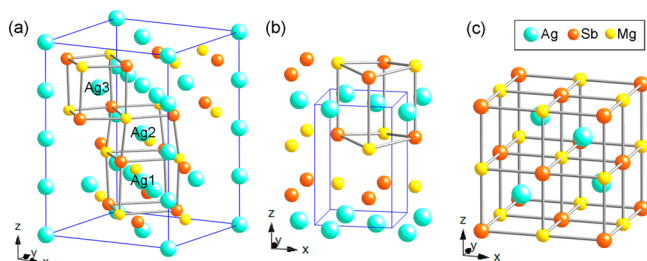

Figure 1. Crystal structures of the (a) low-temperature α-MgAgSb, (b) intermediate β-MgAgSb, and (c) high-temperature γ-MgAgSb, showing Ag atoms located on half of the Mg−Sb polyhedron sites of the distorted or undistorted Mg−Sb rocksalt-type sublattices.

Rietveld refinements were carried out for all the SR-PXRD data measured between 300 and 1000 K, and exemplary plots and data are given in Figure 2 and Table 1. The refinement results show that the as-prepared sample has a single phase of α-MgAgSb at 300 K without any detectable impurities (Figure 2a), indicating that the α-MgAgSb prepared in this work matches the nominal Mg/Ag/Sb ≈ 1:1:1 stoichiometry at room temperature. Trace Sb and Ag_3Sb impurities emerge at elevated temperatures of 400−600 K, and the content of impurities increases with temperature. The concentrations of impurities are 1.1(1) wt % and 2.9(1) wt % for Sb and Ag_3Sb, respectively, at 600 K. Both the β-MgAgSb phase and the γ-MgAgSb phase are observed at 700 K, together with a small amount of the Sb and Ag_3Sb impurities (Figure 2b). The refined concentrations of β-MgAgSb, γ-MgAgSb, Sb, and Ag_3Sb are 53.8(3) wt %,

34.4(3) wt %, 1.9(1) wt %, and 9.9(1) wt %, respectively, at 700 K. Since only Sb and Ag are present as impurities, it can be concluded that β-MgAgSb presumably deviates from the nominal stoichiometric ratio. Therefore, a relative excess of Mg or the presence of Ag and Sb vacancies in the β-MgAgSb is likely, resulting in defects and disorder in the structure. A further refinement of the occupancies of Ag and Sb in β-MgAgSb at 700 K results in a formula unit of $MgAg_{0.87}Sb_{0.94}$, that is, silver and antimony vacancies occur in the crystal, corroborating the appearance of Sb and Ag_3Sb impurities. The full structural details of β-MgAgSb with and without the refinement of Ag and Sb occupancies are given in the Supporting Information (Table S2). The SR-PXRD data at 800 K and above can be modeled using the cubic γ-MgAgSb structure (structural model type I with Mg, Ag, and Sb on the 4b, 4c, and 4a sites, respectively), and no other crystalline impurity phases are found at these temperatures (Figure 2c). By focusing on the high angle data (see Figure 2 insets), the diffraction signals become weak above 55° at 300 K, and no high angle diffraction peaks are distinguishable above 45° at 700 K or above. This is consistent with an increase of the atomic displacement parameters (ADPs) with increasing temperature. The theoretical density of γ-MgAgSb (800 K) is calculated to be 5.598 g/cm^3, which is remarkably smaller than 6.326 g/cm^3 for α-MgAgSb (300 K) and 6.260 g/cm^3 for β-MgAgSb (700 K), assuming that all the three structures are ideal crystal structures without any defects and disorder. This shows that there is a large density change during the phase transformation from β-MgAgSb to γ-MgAgSb.

The SR-PXRD diffraction patterns between 800 and 1000 K show two very broad peaks at ∼7.2° and ∼12.1° as shown in Figure 3a, suggesting that there is an amorphous phase or that an increase of thermal diffuse scattering (TDS) occurs. The amorphous phase can be attributed to melting of Ag_3Sb and Sb
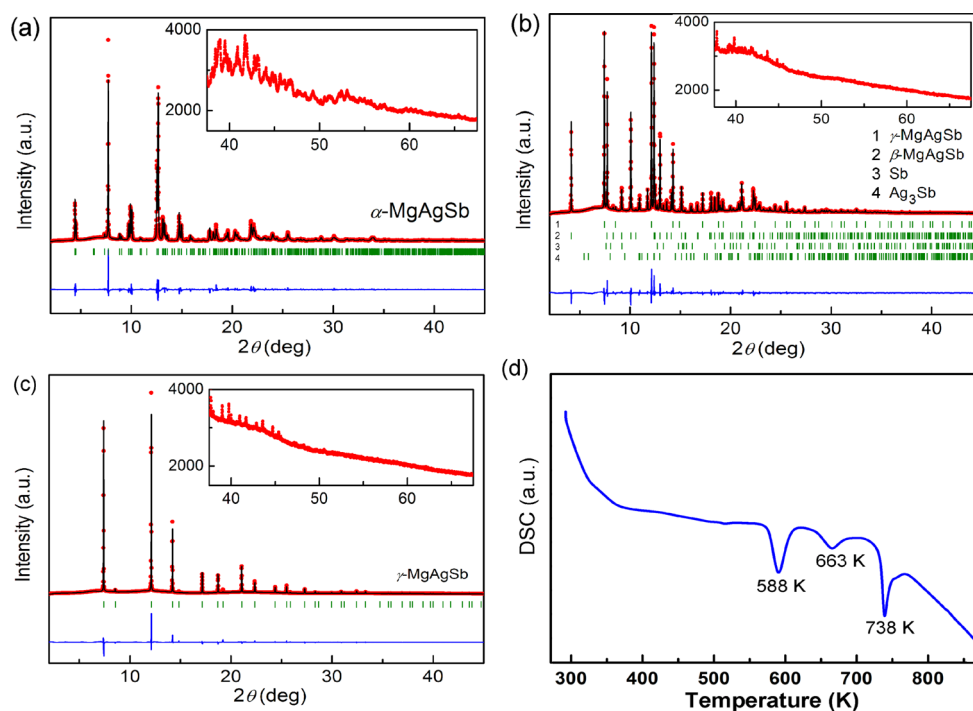

Figure 2. Observed (red) and calculated (black) diffraction patterns and difference profiles (blue) of MgAgSb at (a) 300 K, (b) 700 K, and (c) 800 K (with structural model type I). The insets show the high angle features of the SR-PXRD data. (d) DSC curve showing the endothermic peaks at 588 K, 663 K, and 738 K.

Table 1. Refined Parameters and Crystallographic Details from the Rietveld Analysis of the SR-PXRD Data of MgAgSb at 300, 700, and 800 K

phase	α-MgAgSb	β-MgAgSb	γ-MgAgSb	Sb	Ag$_3$Sb	γ-MgAgSb
temperature (K)	300	700				800
no. data points	7794	7796				7797
no. refined parameters	97	78				64
R_P (%)	11.6	13.1				20.2
R_{WP} (%)	14.1	12.1				15.9
space group	$I\text{-}4c2$	$P4/nmm$	$F\text{-}43m$	$R\text{-}3m$	$Pmm2$	$F\text{-}43m$
no. reflns	1815	236	58	139	266	59
R_I (%)	3.17	4.94	4.17	10.4	8.84	8.25
R_F (%)	1.27	5.82	5.10	8.26	7.95	6.94
a (Å)	9.1631(2)	4.4216(1)	6.6847(1)	4.3173(3)	4.8902(1)	6.7038(1)
b (Å)	9.1631(2)	4.4216(1)	6.6847(1)	4.3173(3)	3.0220(1)	6.7038(1)
c (Å)	12.701(1)	6.8923(1)	6.6847(1)	11.335(1)	5.2755(2)	6.7038(1)
density (g/cm^3)	6.326	6.258	5.646	6.630	9.486	5.598
phase fraction (%)	100	53.8(3)	34.4(3)	1.9(1)	9.9(1)	100
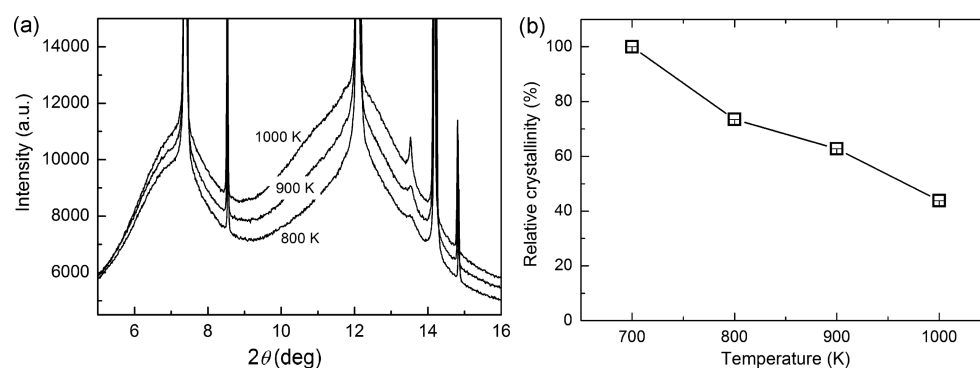
Figure 3. (a) Details of the SR-PXRD diffraction patterns of γ-MgAgSb at 800, 900, and 1000 K, showing an increase of the liquid content with temperature. (b) Relative crystallinity of MgAgSb (assuming the total material at 700 K has 100% crystallinity) showing the dissolution of γ-MgAgSb at high temperatures.

impurities, which were detected at lower temperatures. The Ag–Sb phase diagram[33] shows that the invariant equilibrium point of Ag$_3$Sb + Sb = L is about 753 K, indicating that the impurities are liquefied above 753 K. The phase transformations were further checked by DSC analysis. The DSC curve of MgAgSb (Figure 2d) shows endothermic peaks at 588 and 663 K, corresponding to phase transitions from α-MgAgSb to β-MgAgSb and from β-MgAgSb to γ-MgAgSb, respectively. The endothermic peak at 738 K denotes the melting of Ag$_3$Sb and Sb impurities, in good agreement with the SR-PXRD results. This shows that γ-MgAgSb has a higher melting point as it is present even at 1000 K. The intensities of the amorphous peaks increase with temperature, indicating an increase in the liquid content. This can be attributed to γ-MgAgSb continuously being decomposed at high temperatures. For simple description, we assume that the total material at 700 K has 100% crystallinity. As γ-MgAgSb accounts for 34.4 wt % of the material at 700 K, it contributes 34.4% of the crystallinity. The relative crystallinities of γ-MgAgSb at 800, 900, and 1000 K can be calculated by comparing the refined scale factors of the γ-MgAgSb phase relative to that determined at 700 K (Figure 3b). Thus, the crystallinity of γ-MgAgSb at 800 K is below 75% relative to that at 700 K, and there is only 43.8% crystallinity at 1000 K. From this, we can suggest that γ-MgAgSb is likely to be stable over a larger temperature range if the impurities can be eliminated, making it potentially useful for practical application.

3.2. Atomic Bonds and Structural Disorder in α-MgAgSb. Figure 4a shows the refined cell parameters of α-MgAgSb as functions of temperature. Both cell parameters a and c show linear thermal expansion, but α-MgAgSb exhibits anisotropic thermal expansion behavior with the thermal expansion coefficients of $1.23(1) \times 10^{-5}$ K^{-1} and $2.54(2) \times 10^{-5}$ K^{-1} for a and c directions, respectively. This demonstrates the anisotropic evolution of the α-MgAgSb structure with temperature. As discussed previously, α-MgAgSb can be described as a distorted Mg–Sb rocksalt sublattice by rotating the conventional structure 45° about the c axis.[13] The Mg–Sb rocksalt sublattice is equivalent to the tetragonal sublattice as described in Figure 4b. There are three types of Ag atoms in α-MgAgSb: Ag1 atoms are located on the corners of the lattice, Ag2 atoms on the lattice edges of the c' axis, and Ag3 atoms on the lattice edges of the a' and b' axes. The Mg$_4$Sb$_4$ distorted hexahedron is located in the cage formed by the Ag atoms. Figure 4c shows the unit cell parameters of the tetragonal sublattice (a' and c'), which are calculated from the conventional lattice parameters (a and c): $a' = a/\sqrt{2}$, and $c' = c/2$.[13] It can be seen that the Ag2 atoms are located on the centers of the c' edges of the unit cell, while the Ag3 atoms deviate from the centers of the a' (or b') edges. The distorted Ag3 atoms result in a larger unit cell parameter of a' than c'. However, α-MgAgSb shows a larger thermal expansion along c' than a', which indicates a tendency to increase the structural symmetry with temperature. Actually, as shown in Figure 4d,
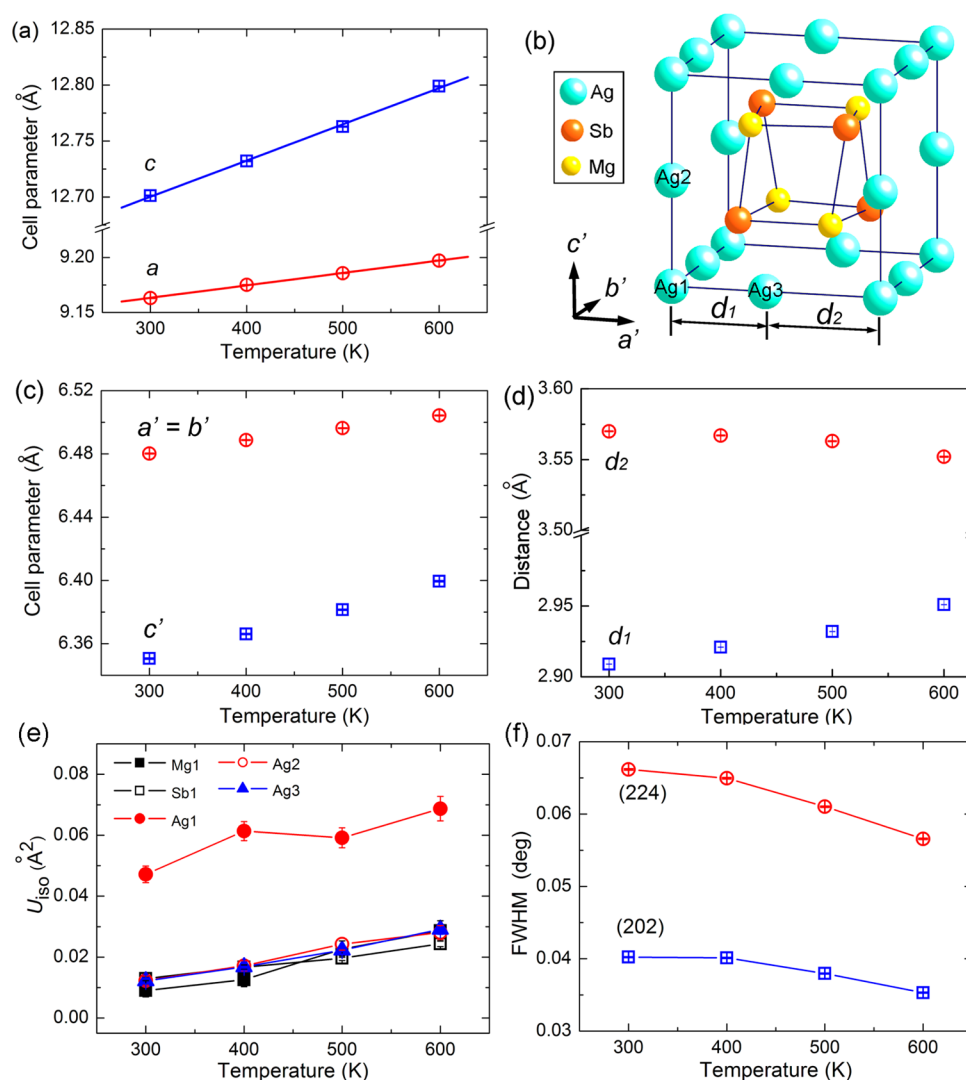
Figure 4. (a) Temperature dependences of unit cell parameters a and c of α-MgAgSb. The solid lines show the linear fits of the thermal expansions. (b) Tetragonal sublattice showing Mg_4Sb_4 distorted hexahedron located in the cage formed by the Ag atoms. (c) Temperature dependences of unit cell parameters a' and c' of α-MgAgSb with the tetragonal sublattice. (d) Temperature dependences of the two neighboring Ag1–Ag3 distances (d_1 and d_2). (e) Temperature dependence of isotropic ADPs (U_{iso}) for different atoms. (f) Full-width at half-maximum (fwhm) values of the (202) and (224) peaks of α-MgAgSb as functions of temperature.

Table 2. Fractional Coordinates and Refined Isotropic ADPs (U_{iso}) of α-MgAgSb at 300 K

atom	site	x	y	z	U_{iso} (Å^2)	occ (%)
Mg1	16i	−0.0215(9)	0.2808(8)	0.1144(5)	0.009(2)	100
Sb1	16i	0.2353(2)	0.4755(2)	0.1164(1)	0.013(1)	100
Ag1	4a	0	0	0.25	0.047(3)	100
Ag2	4b	0	0	0	0.012(1)	100
Ag3	8e	0.2262(3)	0.2262(3)	0.25	0.013(1)	100

the shorter neighboring Ag1–Ag3 distance d_1 increases with temperature, while the longer neighboring Ag1–Ag3 distance d_2 slightly decreases with temperature. Such temperature dependent structure change has normally not been included in the theoretical calculations, while actually it may significantly influence the temperature dependent thermoelectric properties. Moreover, it should be noted that the distortion of the Mg–Sb rocksalt sublattice originates mainly from the a,b-plane, whereas it is less distorted along the c direction since the Mg and Sb atoms have almost identical z coordinates of 0.1132(5) Å and 0.1166(1) Å, respectively, at 300 K. The more distorted atomic

arrangement of the a,b-plane results in the lower thermal expansion coefficient along the a,b-plane compared to that of the c direction. Table 2 and Table S1 list the fractional coordinates of α-MgAgSb at different temperatures.

In the α-MgAgSb structure, the Ag1, Ag2, and Ag3 atoms are located in different Mg_4Sb_4 distorted hexahedra (Figure 1a), forming a variety of chemical bonds with different lengths. Compared with the rigid bond of 2.903 Å for Ag–Sb (or Mg–Ag) in γ-MgAgSb at high temperature of 800 K, weaker bonds are found in α-MgAgSb at the much lower temperature of 300 K due to the change of coordination number. For example, in

Table 3. Refined Isotropic ADPs (U_{iso}) of γ-MgAgSb at 700, 800, 900, and 1000 K Using Type I Model and Type II Models[a]

structure	atom	site (x, y, z)	U_{iso} (Å²) (700 K)	U_{iso} (Å²) (800 K)	U_{iso} (Å²) (900 K)	U_{iso} (Å²) (1000 K)	occ (%)
type I	Mg1	4b (0.5, 0.5, 0.5)	0.063(4)	0.065(4)	0.105(5)	0.166(7)	100
	Ag1	4c (0.25, 0.25, 0.25)	0.025(1)	0.029(1)	0.037(1)	0.041(1)	100
	Sb1	4a (0, 0, 0)	0.081(2)	0.098(2)	0.099(2)	0.119(3)	100
type II	Mg1	4a (0, 0, 0)	0.042(5)	0.044(5)	0.069(8)	0.098(9)	100
	Ag1	4b (0.5, 0.5, 0.5)	0.078(4)	0.095(4)	0.115(5)	0.153(7)	100
	Sb1	4c (0.25, 0.25, 0.25)	0.033(1)	0.037(1)	0.042(1)	0.046(1)	100

[a]R_P = 20.2%, R_{wp} = 15.9%, R_I = 8.25%, and R_F = 6.94% at 800 K for type I model, and R_P = 19.9%, R_{wp} = 15.8%, R_I = 8.53%, and R_F = 5.84% at 800 K for type II model.

the Mg_4Sb_4 distorted hexahedron filled with Ag1 in α-MgAgSb, there are four Ag1−Mg bonds with lengths of 3.124 Å and four Ag1−Sb bonds of 2.965 Å. These are much weaker compared with the rigid bond in γ-MgAgSb. It was reported that the weak bonds will result in a soft phonon mode and strong phonon vibrations during the heat conduction, which is suggested to be the origin of ultralow lattice thermal conductivity in SnSe.[34] Recently, the hierarchical chemical bondings were reported and suggested to be responsible for the intrinsically low lattice thermal conductivity of α-MgAgSb,[12] which is in good agreement with the present results. The ADPs of the atoms are refined with the absorption correction included,[35] where the ADPs represent the atomic thermal vibration plus potential contributions from atomic disorder. For simplicity, isotropic ADP values (U_{iso}) are refined (see Figure 4e, Table 2, and Table S1). Interestingly, it can be seen that the ADP for the Ag1 atom located on 4a (0, 0, 0.25) is rather larger than those of other atoms for all the measured temperatures from 300−600 K. This suggests that Ag1 in 4a might be statically or dynamically disordered. We have extrapolated the ADPs of Ag1 to 0 K, and it seems that there is large static disorder for the Ag1 atoms (Figure S1). The probability density functions of the Ag atoms at different temperatures also suggest large static disorder for Ag1 since for this atom they do not change much with temperature (Figure S2). Refinement of the atomic occupancies leads to deviations no larger than 1% from the stoichiometric value, which does not support the presence of significant antisite defects. On the basis of the above analysis, the presence of weak chemical bonds as well as the large ADP for Ag1 atom could contribute to the low lattice thermal conductivity of α-MgAgSb.

Apparent peak broadening was found for the diffraction data indicating the presence of large microstrain, and the refinement of anisotropic strain is necessary in the Rietveld refinement. The peak broadening was analyzed to investigate the microstrain, which could be generated during the spark plasma sintering of the sample. The full-width at half-maximum (fwhm) values for the (202) and (224) reflections decrease with temperature indicating a relief of microstrain (Figure 4f). It can be seen that only little microstrain is relieved from 300−400 K. The microstrain relief increases at higher temperatures as the fwhm values decrease more rapidly above 400 K.

3.3. Structure of γ-MgAgSb. γ-MgAgSb has the half-Heusler structure, where half-Heusler compounds are a remarkable class of equiatomic ternary intermetallic materials that are considered to be rich in physical properties.[36,37] Half-Heusler materials have a cubic structure with space group of F-43m, and the occupied Wyckoff positions are 4a (0, 0, 0), 4b (0.5, 0.5, 0.5), and 4c (0.25, 0.25, 0.25). There are two different types of atomic ordering observed for half-Heusler compounds.[36] For most half-Heusler compounds, such as MgCuSb,

the Mg, Cu, and Sb atoms are located at 4b, 4c, and 4a positions, respectively (denoted as type I in the present study). However, in the case of MgAgAs, the atomic arrangement is Mg (4a), Ag (4b), and As (4c) (type II). In an earlier study, γ-MgAgSb has been described as the first case where Mg, Ag, and Sb occupy the 4b, 4c, and 4a sites, respectively.[13] However, inconsistent thermoelectric properties are obtained by theoretical calculations and in experimental studies.[15] Theoretical calculations show that γ-MgAgSb has a metallic character, while experimental studies suggest that it behaves as a semiconductor. The low predicted Seebeck coefficients of γ-MgAgSb contrast with the large experimental values. Moreover, as will be discussed in the following part, a very low thermal conductivity is observed for γ-MgAgSb with a glassy feature. As a result, it is important to verify the structure and structural disorder of γ-MgAgSb.

The structure of γ-MgAgSb at 800 K was refined in two ways: first, with Mg, Ag, and Sb on the 4b, 4c, and 4a sites (type I, Figure 2c), and second with Mg, Ag, and Sb on the 4a, 4b, and 4c sites, respectively (type II, Figure S3). The reliability R values are R_P = 20.2%, R_{wp} = 15.9%, R_I = 8.25%, and R_F = 6.94% for the first model, and R_P = 19.9%, R_{wp} = 15.8%, R_I = 8.53%, and R_F = 5.84% for the second model. The refined isotropic ADPs for both models at different temperatures are shown in Table 3. Similar agreement factors are obtained when refining the data using the two structural models, mainly due to the very similar scattering factors of Ag and Sb. The relatively large reliability R values suggest that γ-MgAgSb may not be modeled perfectly by either of the two structures. This could be due to the fact that γ-MgAgSb is highly disordered.

Here, we use the MEM to further analyze γ-MgAgSb with the two structural models: type I (Mg in 4b, Ag in 4c, and Sb in 4a) and type II (Mg in 4a, Ag in 4b, and Sb in 4c positions). MEM is a powerful tool to reconstruct the electron/nuclear density from X-ray/neutron diffraction data.[25] Per se, MEM does not require any structural model that is assumed a priori in a conventional refinement, for example, in the Rietveld refinement. However, in the present case, due to the lack of the center of inversion in F-43m, an initial bias on the phase of the structure factors is imposed and such bias depends not only on the atomic arrangement, but also on the ADPs in the Rietveld refinement. A further complication is given by the relatively low q-resolution and high thermal diffuse scattering that are inherent to high temperature data. Because of these complications and the possible presence of more than one minimum in the least-squares procedure, our analysis is limited to γ-MgAgSb at 800 K, which is phase-pure and for which the data show a better signal-to-noise ratio than at higher temperatures.

Given that the type I and type II models can equally fit the data, MEM calculations were performed using structure factors

extracted and phased according to the type I and type II models. For the type II structural model, we found two minima in the least-squares Rietveld refinement with similar agreement factors. One of the minima gives surprisingly noise-free MEM density maps and it is reported here, while the MEM density obtained from the second minimum is shown in the Supporting Information (Figure S4). The standard deviations of the structure factors extracted with type I and type II differ; therefore, we simply compare the MEM density computed at the lowest χ^2 value obtainable, that is, $\chi^2 = 5.12$ for type I and $\chi^2 = 1$ for type II. The MEM electron density maps corresponding to type I and type II rietveld refinements are shown in Figure 5
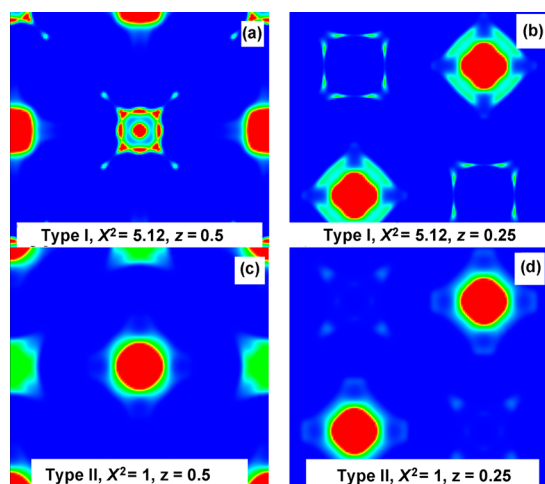
in the (001) plane of the cubic cell at $z = 0.5$ and $z = 0.25$ in fractional coordinates. It is evident that extraction of the structure factors with type II (Figure 5c and 5d) leads to a lower noise level and better atomic electron density shapes than in type I (Figure 5a and 5b), which produces large noise levels and a completely unphysical charge density of the Mg atom in the $4b$ position. Actually, the noise level in the type I MEM density decreases if the calculation is stopped at higher χ^2 values inferring that the noise level might partly be due to overfitting of the data rather than real inconsistencies of the phases of the structure factors (see Figure S5). It is instructive to notice that in the MEM calculations, type II could be a possible candidate for the structure. However, as discussed further, structural disorder should be considered to further interpret the detailed structure of γ-MgAgSb.

3.4. Structural Disorder of γ-MgAgSb. The above analysis shows that γ-MgAgSb cannot be modeled perfectly by either the type I or type II structural models, and this could be due to the presence of structural disorder. It is worth noting that the temperature dependence of the cell parameter of γ-MgAgSb deviates from a linear relationship (Figure 6c) indicating a continuous change of the composition of γ-MgAgSb during heating. The appearance of Ag_3Sb and Sb impurities at high temperatures (which are melted above 800 K) indicates Mg excess or Ag and Sb deficiencies in γ-MgAgSb, resulting in structural disorder. The above MEM analysis shows that the type II structure gives a more physically sound MEM electron density, and we therefore use the type II model for a further interpretation of the structural disorder in γ-MgAgSb.

First, we estimate the occupancies of γ-MgAgSb using the type II model. The ADPs of γ-MgAgSb at different temperatures in ordered structure of type II model (Table 3) show that the Mg and Ag sites have relatively large ADPs, while Sb site has normal ADPs. This suggests that the disorder is more likely to be present on the Mg and Ag sites, while the Sb sublattice forms an anion framework. Thus, we fix the occupancy of Sb to unity and fix the ADPs for each atom

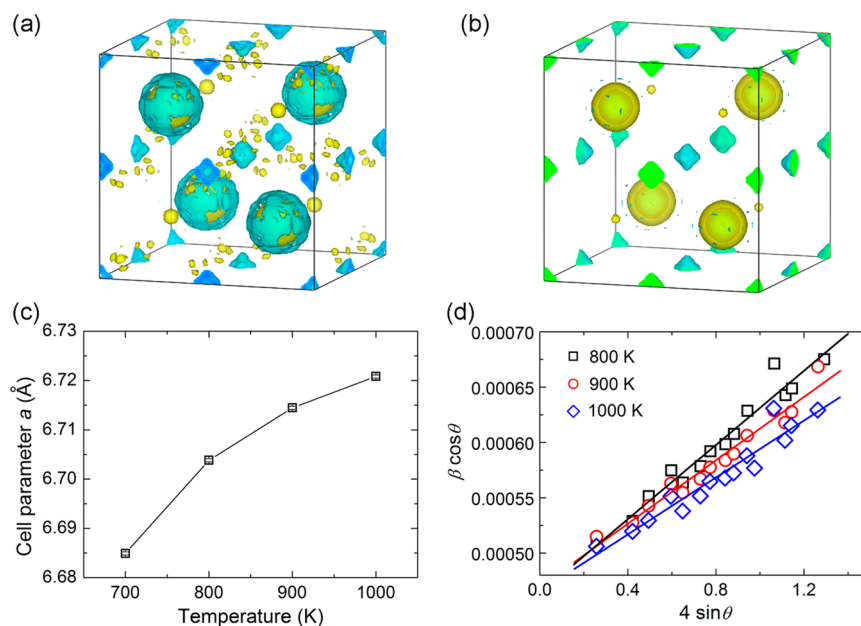**Figure 5.** MEM electron densities at 800 K using structure factor extracted with (a, b) type I and (c, d) type II structural models of γ-MgAgSb. In all maps, the plane (001) is considered at $z = 0.5$ and $z = 0.25$ in fractional coordinates. The color scale is set from 0 (blue) to 15 eÅ^{-3} (red).

Figure 6. (a) Fourier difference of the data at 800 K using type II structural model of γ-MgAgSb where Mg, Ag, and Sb occupy $4b$, $4c$, and $4a$ sites, respectively (isosurface level 2.5 eÅ^{-3}). (b) Fourier difference of the data at 800 K using type II structural model with the occupancies of Mg and Ag refined (isosurface level 2.5 eÅ^{-3}). (c) Cell parameter of γ-MgAgSb as a function of temperature. (d) Williamson−Hall analysis of γ-MgAgSb.

based on the ordered structure while refining the occupancies of Mg and Ag. The refinement gives improved agreement factors of R_P = 19.2%, R_{wp} = 14.7%, R_I = 6.87%, and R_F = 5.71% at 800 K. The Fourier difference map at 800 K also shows large improvement in the description of the data with the occupancies refined compared with the ordered structure (Figure 6a,b). The refinements reveal that the composition of γ-MgAgSb changes with temperature, and refined compositions of $Mg_{1.18}Ag_{0.80}Sb$, $Mg_{1.39}Ag_{0.72}Sb$, $Mg_{1.50}Ag_{0.63}Sb$, and $Mg_{1.60}Ag_{0.54}Sb$ are obtained at 700, 800, 900, and 1000 K, respectively (Table S3). The refined compositions agree with the increasing amount of primary impurity of Ag_3Sb phase at high temperature. However, the refined compositions deviate too much from the stoichiometric ratio of γ-MgAgSb; the occupancy of Mg exceeds unity, and the Ag vacancy concentration is too high. This is not likely to be true for γ-MgAgSb. Instead, it is more likely that the Mg and Ag sites mix, leading to increased scattering power on the Mg site (occupancy above unity) and decreased scattering power on the Ag site (presumed high vacancy concentration).

The γ-MgAgSb crystal structure can also be described as a CaF_2 structure with space group $Fm\text{-}3m$ where Mg and Ag sit randomly on 8c, and the Sb atoms sit on 4a (Table 4). Here,

Table 4. Refined Parameters of γ-MgAgSb Using the CaF_2 Structure with Space Group of $Fm\text{-}3m$ at 800, 900, and 1000 K[a]

temp (K)	atom	site (x, y, z)	U_{iso} (Å²)	occ (%)
800	Mg1	8c (0.25, 0.25, 0.25)	0.094(1)	61(1)
	Ag1	8c (0.25, 0.25, 0.25)	0.094(1)	39(1)
	Sb1	4a (0, 0, 0)	0.046(1)	100
900	Mg1	8c (0.25, 0.25, 0.25)	0.107(2)	67(1)
	Ag1	8c (0.25, 0.25, 0.25)	0.107(2)	33(1)
	Sb1	4a (0, 0, 0)	0.053(1)	100
1000	Mg1	8c (0.25, 0.25, 0.25)	0.122(3)	74(1)
	Ag1	8c (0.25, 0.25, 0.25)	0.122(3)	26(1)
	Sb1	4a (0, 0, 0)	0.060(1)	100

[a]Occupancies of Mg1 and Ag1 at 8c are constrained to the total value of 100%. R_P = 17.1%, R_{wp} = 13.3%, R_I = 3.98%, and R_F = 4.05% at 800 K.

the occupancies of Mg and Ag at 8c are constrained to 100%. The CaF_2 structure description significantly improves the refinement based on the R factors: R_P = 17.1%, R_{wp} = 13.3%, R_I = 3.98%, and R_F = 4.05%. Refined compositions of $Mg_{1.22}Ag_{0.78}Sb$, $Mg_{1.34}Ag_{0.66}Sb$, and $Mg_{1.48}Ag_{0.52}Sb$ are obtained at 800, 900, and 1000 K, respectively. These agree with the increasing amount of primary impurity of Ag_3Sb phase at high temperature. It should be noted that the chemical valence of the refined compositions is not balanced. To achieve balance of the chemical valence, some Mg or Ag vacancies at the 8c site are required in the structure. It is not possible to refine the occupancies of Mg and Ag separately due to parameter correlation, and it is therefore impossible to further model the disordered structure with vacancies. Nonetheless, the refined compositions suggest the presence of disorder in γ-MgAgSb. Overall, mixed sites of Mg and Ag as well as vacancies are suggested to constitute the disorder of γ-MgAgSb. The vacancy concentration should increase with temperature for the purpose of valence balance, resulting in the nonlinear relationship of the temperature dependence of unit cell parameter. Moreover, this is indicative that γ-MgAgSb could be a superionic phase. The

presence of vacancies allow ion diffusion, while the diffusion of the Mg and Ag cations results in the mixed sites. The Sb anion sublattice serves as a framework to stabilize the structure.

Depending on different θ positions, the microstrain (ε) of crystalline γ-MgAgSb can be derived from the instrument-corrected broadening fwhm (β) by Williamson–Hall method in the following equation:[38]

$$\beta \cos \theta = D + 4\varepsilon \sin \theta \tag{1}$$

where D is a constant relative to the size-dependent effect. $\beta \cos \theta$ is plotted with respect to $4 \sin \theta$ for the diffraction peaks (Figure 6d), and it is evident that $\beta \cos \theta$ at each temperature shows a good linear relationship with $4 \sin \theta$, indicating that the microstrain is close to isotropic. The microstrains derived from the slopes are 1.67×10^{-4}, 1.43×10^{-4}, and 1.29×10^{-4} at 800, 900, and 1000 K, respectively, suggesting a relief of microstrain with increasing temperature due to the annealing process.

3.5. Density Functional Theory (DFT) Calculations. DFT calculations were carried out to further analyze the two structural models of γ-MgAgSb. Although it reveals that type I is more stable at 0 K, at the experimental geometries of T > 800 K, the two type structural models are very close in energy inferring that type II is possible as well (Figure S6). Electronic band structure calculations were performed for the two different structural models. Interestingly, the electronic band structure calculation shows that γ-MgAgSb using type I structural model behaves as a metal (Figure 7a), which agrees
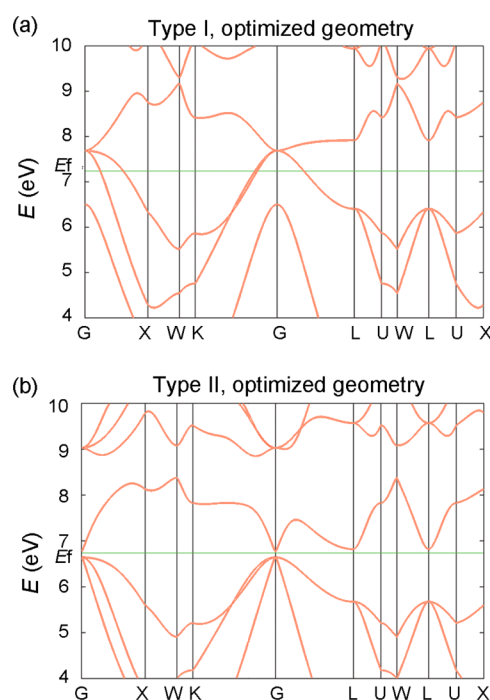

Figure 7. Calculated electronic band structures of γ-MgAgSb using (a) type I and (b) type II structural models.

with the previous theory calculations.[15] On the other hand, γ-MgAgSb using the type II structural model is a narrow gap semiconductor (Figure 7b), which agrees with the experimental results which will be discussed later. However, we performed calculations of phonon dispersion and found that type II structural model produces imaginary frequencies (Figure S7), that is, the structure is not a minimum in the atomic potential energy surface. Theory thus suggests that the type II structural

model is not mechanically stable, or that the structure may be highly disordered. As discussed above, Rietveld refinements have shown that γ-MgAgSb is likely to be a superionic phase with the presence of vacancies and disorder of Mg and Ag in a random distribution over the $8c$ site in the CaF_2-type structure. The presence of imaginary frequencies for the DFT calculations of type II structural model is very similar to that found in superionic phase of copper selenide with antifluorite crystal structure.[39−41]

3.6. Thermoelectric Properties.
Figure 8 displays the thermoelectric properties as functions of temperature between
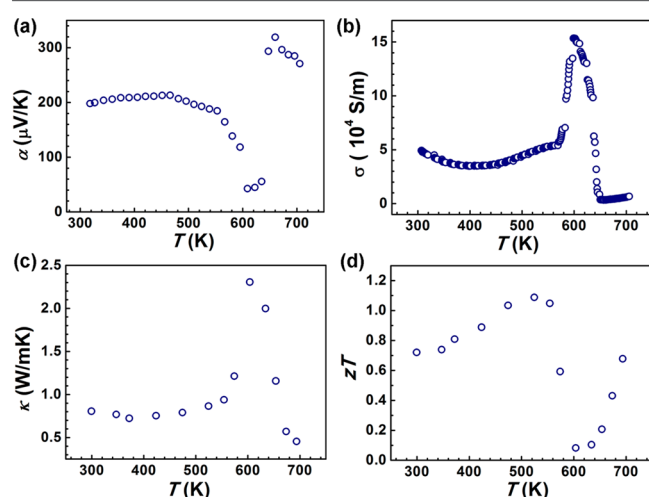
Figure 8. Temperature dependences of (a) the Seebeck coefficient α, (b) the electrical conductivity σ, (c) the thermal conductivity κ, and (d) the dimensionless figure of merit zT of MgAgSb in the temperature range between 300 and 710 K.

300 and 700 K. Discontinuous changes at about 580 and 650 K are observed in the Seebeck, α, electrical conductivity, σ, and thermal conductivity, κ. The room temperature phase α-MgAgSb shows very promising thermoelectric properties with a maximum zT value of about 1.1 at 520 K. Very low thermal conductivity of $\kappa = 0.8$ W/mK is obtained for α-MgAgSb. The intermediate phase β-MgAgSb has a high electrical conductivity, a high thermal conductivity, and a low Seebeck coefficient, representing a metallic behavior. γ-MgAgSb has a very high Seebeck coefficient with a value of 285 μV/K at 700 K, a relatively low electrical conductivity of 0.54×10^4 S/m at 700 K, and a very low thermal conductivity of 0.45 W/mK at 700 K. A highest zT value of about 0.68 is obtained for γ-MgAgSb at 700 K in the measured temperature range. The high-temperature phase γ-MgAgSb clearly shows a semiconductor behavior. As discussed above, theoretical calculations indicate that γ-MgAgSb with type I structural model has a metallic character, while γ-MgAgSb with type II structural model is a narrow gap semiconductor. From this point of view, the type II structural model seems correct and in much better agreement with the experimental transport measurements than the type I structure. This conclusion is further corroborated by the noise free MEM map obtained with the type II model, although it should be noted that the structure may be highly disordered. It should be noted that MgAgSb is supposed to be used only at low temperature rather than above the phase transitions because the lifetime and cyclability of a thermoelectric module otherwise will be strongly limited.

A rapid change in thermoelectric properties has also been observed for other materials. It was found that $Ag_{10}Te_4Br_3$ is capable of switching semiconducting properties with a drastic change observed in Seebeck coefficient.[42] It was suggested that the silver and tellurium substructures show different stages of disorder in the polymorphs, resulting different silver mobility during the phase transition. In the case of In_4Se_3, a sharp dip of Seebeck coefficient was suggested to be due to the melting of the excess indium, and the disordered structure with strong electron−phonon coupling was attributed to the promising thermoelectric properties.[43] In the present study, the discontinuous changes of the thermoelectric properties show that MgAgSb changes from semiconductor to metal and back to semiconductor with increasing temperature, corresponding to the different phase transitions, in good agreement with the DSC and SR-PXRD results. MgAgSb tends to slightly decompose at high temperatures with increasing amounts of Ag_3Sb and Sb impurities, resulting in different stages of disorder in MgAgSb at different temperatures. The different stages of disorder in the MgAgSb polymorphs as well as the impurities should cause the large differences in thermoelectric properties. The very low thermal conductivity of α-MgAgSb can be explained by the weak chemical bonds and large atomic disorder. β-MgAgSb behaves as a metal, and the presence of metallic imurities should also affect the properties. In γ-MgAgSb, there are large amounts of vacancies and strong disorder of mixed Mg and Ag in the cation sublattice. The very low thermal conductivity of γ-MgAgSb at high temperature (0.45 W/mK at 700 K) can be attributed to the strong disorder of the cation sublattice with "phonon liquid" features.

4. CONCLUSIONS

The crystal structure and structural disorder of MgAgSb have been studied by multitemperature high-resolution synchrotron radiation powder X-ray diffraction. α-MgAgSb prepared in this work is in agreement with the nominal stoichiometric ratio at room temperature. Trace impurities of Sb and Ag_3Sb appear at elevated temperatures of 400−600 K, and the impurity content increases with temperature. Weak chemical bonds and large atomic disorder are found for α-MgAgSb contributing to the low thermal conductivity of this material. A tendency of increasing structural symmetry with temperature is observed for α-MgAgSb, which may significantly contribute to the temperature evolution of the thermoelectric properties. The high resolution powder data of γ-MgAgSb can be fitted using both type I (with Mg, Ag, and Sb on the $4b$, $4c$, and $4a$ sites, respectively) and type II (with Mg, Ag, and Sb on the $4a$, $4b$, and $4c$ sites, respectively) half-Heusler crystal structure models. MEM analysis carried out on the extracted factors shows that type II gives a more physically reasonable electron density. The very low thermal conductivity of γ-MgAgSb is attributed to the strong disorder of the cation sublattice with "phonon liquid" feature. The high temperature transport data suggest a semiconducting γ-MgAgSb phase in agreement with theoretical calculation for the type II structure.

■ ASSOCIATED CONTENT

ⓢ Supporting Information

The Supporting Information is available free of charge on the ACS Publications website at DOI: 10.1021/acs.chemmater.7b01768.

Additional results from Rietveld refinements, MEM charge densities, DFT calculations, and phonon calculations ([PDF](#))

■ AUTHOR INFORMATION

Corresponding Authors
*E-mail: jlmi@ujs.edu.cn.
*E-mail: zhutj@zju.edu.cn.
*E-mail: bo@chem.au.dk.
ORCID ⊕
Tie-Jun Zhu: 0000-0002-3868-0633
Bo Brummerstedt Iversen: 0000-0002-4632-1024
Notes
The authors declare no competing financial interest.

■ REFERENCES

(1) DiSalvo, F. J. Thermoelectric Cooling and Power Generation. *Science* **1999**, *285*, 703−706.

(2) Zhu, T.; Liu, Y.; Fu, C.; Heremans, J. P.; Snyder, J. G.; Zhao, X. Compromise and Synergy in High-Efficiency Thermoelectric Materials. *Adv. Mater.* **2017**, *29*, 1605884.

(3) Venkatasubramanian, R.; Siivola, E.; Colpitts, T.; O'Quinn, B. Thin-Film Thermoelectric Devices with High Room-Temperature Figures of Merit. *Nature* **2001**, *413*, 597−602.

(4) Poudel, B.; Hao, Q.; Ma, Y.; Lan, Y.; Minnich, A.; Yu, B.; Yan, X.; Wang, D.; Muto, A.; Vashaee, D.; Chen, X.; Liu, J.; Dresselhaus, M. S.; Chen, G.; Ren, Z. High-Thermoelectric Performance of Nanostructured Bismuth Antimony Telluride Bulk Alloys. *Science* **2008**, *320*, 634−638.

(5) Boukai, A. I.; Bunimovich, Y.; Tahir-Kheli, J.; Yu, J.-K; Goddard, W. A., III; Heath, J. R. Silicon Nanowires as Efficient Thermoelectric Materials. *Nature* **2008**, *451*, 168−171.

(6) Tan, G.; Zhao, L. D.; Kanatzidis, M. G. Rationally Designing High-Performance Bulk Thermoelectric Materials. *Chem. Rev.* **2016**, *116*, 12123−12149.

(7) Shuai, J.; Kim, H. S.; Lan, Y.; Chen, S.; Liu, Y.; Zhao, H.; Sui, J.; Ren, Z. Study on Thermoelectric Performance by Na Doping in Nanostructured $Mg_{1-x}Na_xAg_{0.97}Sb_{0.99}$. *Nano Energy* **2015**, *11*, 640−646.

(8) Liu, Z.; Shuai, J.; Mao, J.; Wang, Y.; Wang, Z.; Cai, W.; Sui, J.; Ren, Z. Effects of Antimony Content in $MgAg_{0.97}Sb_x$ on Output Power and Energy Conversion Efficiency. *Acta Mater.* **2016**, *102*, 17−23.

(9) Kraemer, D.; Sui, J.; McEnaney, K.; Zhao, H.; Jie, Q.; Ren, Z. F.; Chen, G. High Thermoelectric Conversion Efficiency of MgAgSb-Based Material with Hot-Pressed Contacts. *Energy Environ. Sci.* **2015**, *8*, 1299−1308.

(10) Liu, Z.; Wang, Y.; Mao, J.; Geng, H.; Shuai, J.; Wang, Y.; He, R.; Cai, W.; Sui, J.; Ren, Z. Lithium Doping to Enhance Thermoelectric Performance of MgAgSb with Weak Electron-Phonon Coupling. *Adv. Energy Mater.* **2016**, *6*, 1502269.

(11) Ying, P.; Liu, X.; Fu, C.; Yue, X.; Xie, H.; Zhao, X.; Zhang, W.; Zhu, T. High Performance α-MgAgSb Thermoelectric Materials for Low Temperature Power Generation. *Chem. Mater.* **2015**, *27*, 909−913.

(12) Ying, P.; Li, X.; Wang, Y.; Yang, J.; Fu, C.; Zhang, W.; Zhao, X.; Zhu, T. Hierarchical Chemical Bonds Contributing to the Intrinsically Low Thermal Conductivity in α-MgAgSb Thermoelectric Materials. *Adv. Funct. Mater.* **2017**, *27*, 1604145.

(13) Kirkham, M. J.; dos Santos, A. M.; Rawn, C. J.; Lara-Curzio, E.; Sharp, J. W.; Thompson, A. J. Ab Initio Determination of Crystal Structures of the Thermoelectric Material MgAgSb. *Phys. Rev. B: Condens. Matter Mater. Phys.* **2012**, *85*, 144120.

(14) Zhao, H.; Sui, J.; Tang, Z.; Lan, Y.; Jie, Q.; Kraemer, D.; McEnaney, K.; Guloy, A.; Chen, G.; Ren, Z. High Thermoelectric Performance of MgAgSb-based Materials. *Nano Energy* **2014**, *7*, 97−103.

(15) Miao, N.; Ghosez, P. Optimization of Thermoelectric Properties of MgAgSb-Based Materials: A First-Principles Investigation. *J. Phys. Chem. C* **2015**, *119*, 14017−14022.

(16) Baran, J. D.; Kepaptsoglou, D.; Molinari, M.; Kulwongwit, N.; Azough, F.; Freer, R.; Ramasse, Q. M.; Parker, S. C. Role of Structure and Defect Chemistry in High-Performance Thermoelectric Bismuth Strontium Cobalt Oxides. *Chem. Mater.* **2016**, *28*, 7470−7478.

(17) Christensen, M.; Johnsen, S.; Iversen, B. B. Thermoelectric Clathrates of Type I. *Dalton Trans.* **2010**, *39*, 978−992.

(18) Mi, J. L.; Christensen, M.; Nishibori, E.; Iversen, B. B. Multitemperature Crystal Structures and Physical Properties of the Partially Filled Thermoelectric Skutterudites $M_{0.1}Co_4Sb_{12}$ (M = La, Ce, Nd, Sm, Yb, and Eu). *Phys. Rev. B: Condens. Matter Mater. Phys.* **2011**, *84*, 064114.

(19) Kastbjerg, S.; Bindzus, N.; Søndergaard, M.; Johnsen, S.; Lock, N.; Christensen, M.; Takata, M.; Spackman, M. A.; Iversen, B. B. Direct Evidence of Cation Disorder in Thermoelectric Lead Chalcogenides PbTe and PbS. *Adv. Funct. Mater.* **2013**, *23*, 5477−5483.

(20) Iversen, B. B. Fulfilling Thermoelectric Promises: β-Zn_4Sb_3 from Materials Research to Power Generation. *J. Mater. Chem.* **2010**, *20*, 10778−10787.

(21) Xie, H. H.; Mi, J. L.; Hu, L. P.; Lock, N.; Chirstensen, M.; Fu, C. G.; Iversen, B. B.; Zhao, X. B.; Zhu, T. J. Interrelation between Atomic Switching Disorder and Thermoelectric Properties of ZrNiSn Half-Heusler Compounds. *CrystEngComm* **2012**, *14*, 4467−4471.

(22) Kato, K.; Hirose, R.; Takemoto, M.; Ha, S.; Kim, J.; Higuchi, M.; Matsuda, R.; Kitagawa, S.; Takata, M.; Garrett, R.; et al. The RIKEN Materials Science Beamline at SPring-8. *AIP Conf. Proc.* **2009**, *1234*, 875−878.

(23) Rodriguez-Carvajal, J. Recent Advances in Magnetic Structure Determination Neutron Powder Diffraction. *Phys. B* **1993**, *192*, 55−69.

(24) Petříček, V.; Dušek, M.; Palatinus, L. Crystallographic Computing System JANA2006: General Features. *Z. Kristallogr. - Cryst. Mater.* **2014**, *229*, 345−352.

(25) Sakata, M.; Sato, M. Accurate Structure Analysis by the Maximum-Entropy Method. *Acta Crystallogr., Sect. A: Found. Crystallogr.* **1990**, *46*, 263−270.

(26) van Smaalen, S.; Palatinus, L.; Schneider, M. The Maximum-Entropy Method in Superspace. *Acta Crystallogr., Sect. A: Found. Crystallogr.* **2003**, *59*, 459−469.

(27) Yang, S. H.; Zhu, T. J.; Sun, T.; He, J.; Zhang, S. N.; Zhao, X. B. Nanostructures in High-Performance $(GeTe)_x(AgSbTe_2)_{100-x}$ Thermoelectric Materials. *Nanotechnology* **2008**, *19*, 245707.

(28) Giannozzi, P.; Baroni, S.; Bonini, N.; Calandra, M.; Car, R.; Cavazzoni, C.; Ceresoli, D.; Chiarotti, G. L.; Cococcioni, M.; Dabo, I.; Dal Corso, A.; de Gironcoli, S.; Fabris, S.; Fratesi, G.; Gebauer, R.; Gerstmann, U.; Gougoussis, C.; Kokalj, A.; Lazzeri, M.; Martin-Samos, L.; Marzari, N.; Mauri, F.; Mazzarello, R.; Paolini, S.; Pasquarello, A.; Paulatto, L.; Sbraccia, C.; Scandolo, S.; Sclauzero, G.; Seitsonen, A. P.; Smogunov, A.; Umari, P.; Wentzcovitch, P. M. QUANTUM ESPRESSO: A Modular and Open-Source Software Project for Quantum Simulations of Materials. *J. Phys.: Condens. Matter* **2009**, *21*, 395502.

(29) Blöchl, P. E. Projector Augmented-Wave Method. *Phys. Rev. B: Condens. Matter Mater. Phys.* **1994**, *50*, 17953−17979.

(30) Perdew, J. P.; Burke, K.; Ernzerhof, M. Generalized Gradient Approximation Made Simple. *Phys. Rev. Lett.* **1996**, *77*, 3865−3868.

(31) Baroni, S.; Giannozzi, P.; Testa, A. Green's-Function Approach to Linear Response in Solids. *Phys. Rev. Lett.* **1987**, *58*, 1861−1864.

(32) Setyawan, W.; Curtarolo, S. High-Throughput Electronic Band Structure Calculations: Challenges and Tools. *Comput. Mater. Sci.* **2010**, *49*, 299−312.

(33) Oh, C. S.; Shim, J. H.; Lee, B. J.; Lee, D. N. A Thermodynamic Study on the Ag-Sb-Sn System. *J. Alloys Compd.* **1996**, *238*, 155−166.

(34) Xiao, Y.; Chang, C.; Pei, Y.; Wu, D.; Peng, K.; Zhou, X.; Gong, S.; He, J.; Zhang, Y.; Zeng, Z.; Zhao, L. D. Origin of Low Thermal Conductivity in SnSe. *Phys. Rev. B: Condens. Matter Mater. Phys.* **2016**, *94*, 125203.

(35) Jones, P. G. Crystal Structure Determination: A Critical View. *Chem. Soc. Rev.* **1984**, *13*, 157.

(36) Graf, T.; Felser, C.; Parkin, S. S. P. Simple Rules for the Understanding of Heusler Compounds. *Prog. Solid State Chem.* **2011**, *39*, 1−50.

(37) Zhu, T. J.; Fu, C. G.; Xie, H. H.; Liu, Y. T.; Zhao, X. B. High Efficiency Half-Heusler Thermoelectric Materials for Energy Harvesting. *Adv. Energy Mater.* **2015**, *5*, 1500588.

(38) Zak, A. K.; Majid, W. H. A.; Abrishami, M. E.; Yousefi, R. X-ray Analysis of ZnO Nanoparticles by Williamson-Hall and Size-Strain Plot Methods. *Solid State Sci.* **2011**, *13*, 251−256.

(39) Danilkin, S. A.; Yethiraj, M.; Kearley, G. J. Phonon Dispersion in Superionic Copper Selenide − Observation of Soft Phonon Modes in Superionic Phase Transition. *J. Phys. Soc. Jpn.* **2010**, *79*, 25−28.

(40) Liu, H.; Shi, X.; Xu, F.; Zhang, L.; Zhang, W.; Chen, L.; Li, Q.; Uher, C.; Day, T.; Snyder, G. J. Copper Ion Liquid-Like Thermoelectrics. *Nat. Mater.* **2012**, *11*, 422−425.

(41) Liu, H.; Yang, J.; Shi, X.; Danilkin, S. A.; Yu, D.; Wang, C.; Zhang, W.; Chen, L. Reduction of Thermal Conductivity by Low Energy multi-Einstein Optic Modes. *J. Materiomics* **2016**, *2*, 187−195.

(42) Nilges, T.; Lange, S.; Bawohl, M.; Deckwart, J. M.; Janssen, M.; Wiemhöfer, H. D.; Decourt, R.; Chevalier, B.; Vannahme, J.; Eckert, H.; Weihrich, R. Reversible Switching between P- and N-type Conduction in the Semiconductor $Ag_{10}Te_4Br_3$. *Nat. Mater.* **2009**, *8*, 101−108.

(43) Rhyee, J. S.; Lee, K. H.; Lee, S. M.; Cho, E., II; Kim, S.; Lee, E.; Kwon, Y. S.; Shim, J. H.; Kotliar, G. Peierls Distortion as a Route to High Thermoelectric Performance in $In_4Se_{3-\delta}$ Crystals. *Nature* **2009**, *459*, 965−968.